IL NUOVO CIMENTO **43 C** (2020) 127
DOI 10.1393/ncc/i2020-20127-y

COMMUNICATIONS: SIF Congress 2019

Microbubble whispering gallery mode resonator as an all-optical platform for the characterisation of photoacoustics contrast agents

GABRIELE FRIGENTI([1])([2])([3])(*)

([1]) *Centro Fermi, Museo Storico della Fisica e Centro Studi e Ricerche "Enrico Fermi" Compendio del Viminale, Piazza del Viminale 1, 00184 Roma, Italy*
([2]) *Istituto di Fisica Applicata "Nello Carrara" (IFAC), Consiglio Nazionale delle Ricerche (CNR) - Via Madonna del Piano 10, I50019 Sesto Fiorentino, Italy*
([3]) *Laboratorio Europeo di Spettroscopia Nonlineare (LENS), Università degli Studi di Firenze Via Nello Carrara 1, I50019 Sesto Fiorentino, Italy*

received 29 January 2020

Summary. — This article presents a microbubble resonator (MBR) as an all-optical ultrasound transducer specialized for the characterisation of photoacoustics (PA) contrast agents. In the presented proof-of-concept experiment, a well-known contrast agent (gold nanorods, GNRs) was placed within the MBR and acoustic detection was achieved by monitoring an MBR optical resonance, exploiting the MBR mechanical resonances to enhance the transduction mechanism. The read-out signal from the MBR was validated through a numerical simulation and through the reconstruction of the GNRs photostability trend, proving the feasibility of the characterisation. This work sets the stage for the application of the MBR system to a specific task, taking advantage of its promising features: sensitive PA detection, extremely small volume, ease of integration in a microfluidic circuit, absence of acoustic matching material and scalability.

1. – Introduction

A Whispering Gallery Mode (WGM) resonator is a monolithic dielectric structure with cylindrical symmetry and curved interfaces, with the easiest geometry being the sphere. Due to their geometry and their little size, which ranges from a few millimetres to tens of micrometres, WGM resonators support confined electromagnetic modes,

(*) E-mail: g.frigenti@ifac.cnr.it

for optical and infrared wavelengths [1-3]. These modes are localized in close proximity to the interfaces and extend for fractions of the wavelength into the surrounding medium, allowing light injection and extraction through a waveguide. Despite the numerous possibilities for shape, size and material, WGM micro-resonators fabricated in low-loss materials share the common features of having narrow optical resonances (leading to very high quality factors [4, 5]) and little modal volumes. These features make them interesting for studies in non-linear optics [6, 7], radio-frequency photonics [8, 9] and optical sensing [10-13]. The latter, in particular, is typically achieved by monitoring the shift of a WGM resonance while the perturbation to be quantified (*e.g.*, pressure wave, mechanical stress, chemical action) interacts with the resonator.

The WGM resonator at the core of this work, which falls under the optical sensing applications, is a microbubble resonator (MBR). These resonators are fabricated by inflating a glass capillary while heating it [14-16] and therefore they can be easily filled with liquids by connecting the capillary stem to a microfluidic circuit. This unique property in the WGM landscape allows the implementation of the MBRs as effective sensors for applications in biology and chemistry [17-21]. Additionally, due to their hollow sphere shape and thin glass walls (in the micrometer range or below), MBRs are also high-quality–factors mechanical resonators: another unique feature which makes them very sensitive towards mechanical perturbations [22-25].

The combination of high mechanical sensibility and ability to host liquids makes MBRs particularly promising as acoustic detectors in the field of photoacoustics (PA), which gained interest in recent years for its results in biological and medical applications [26-32]. In a typical PA experiment or device, an optical absorber immersed in a host material is excited by a pulsed resonant laser and de-excites through a complex cascade of thermo-elastic processes, leading to the emission of an acoustic wave (PA wave) [33-35]. By measuring the intensity and the frequency of the PA wave, it is possible to gather information about the optical absorber, such as concentration, size and position. In the case of biomedical applications, one of the most exploited endogenous absorber is the blood cell [36] and the information gathered through the PA response can be used for diagnostic purposes; the host material, instead, is the tissue surrounding the vein/capillary containing the blood cells.

The typical detectors in PA applications are piezoelectric microphones. These detectors allow non-invasive measurements through the aid of an acoustic-matching medium (typically echografic gel) and can be tailored in terms of bandwidth, acceptance angle and sensitivity. This flexibility, however, is limited in terms of size: piezoelectric microphones are hard to miniaturize without severe performance degradation [37]. In order to achieve miniaturisation and competitive performances, optical detection of acoustic waves is being investigated and optical transducers have already demonstrated their effectiveness [37-40].

In this context, I recently collaborated in the implementation of an MBR as an all-optical platform for the characterisation of PA contrast agents [41]. In this configuration the MBR acted as both the vial containing the PA contrast agent and the transducer performing the optical read-out of the PA wave, achieving extreme compactness and sensitive detection. The MBR response was validated by a comparison with a numerical simulation accounting for the cascade of processes leading to PA emission and by the experimental reconstruction of the photostability curve of gold nanorods (GNRs), which are well-known PA contrast agents [42-47]. Additionally, the work proved the effectiveness of transducers which are both optically and mechanically resonant in a non-

imaging PA application. In this paper the implementation is described in detail, giving an in-laboratory perspective to the work.

2. – Setup description

The setup implementing the MBR all-optical system can be conceptually split into three subsystems with the MBR being the junction point of the three (fig. 1(a)): the microfluidic subsystem, which was aimed at filling the MBR with the GNRs; the pump subsystem, which was aimed at triggering the PA wave from the contrast agent (GNRs) in the MBR; the probe subsystem, which was aimed at PA detection through the optical shift induced in a WGM resonance. The MBR used in this experiment was fabricated by an arc discharge tecnique [15], had a 540 μm diameter and a 82 nl internal volume.

The microfluidic subsystem (fig. 1(a)) comprised a set of tubings and a peristaltic pump (Minipuls 3, Gilson, Middleton, WI, USA) to fill the MBR with the GNRs colloidal suspension. A home-made holder was designed to handle the MBR during the connection of the tubings and keep its position stable during the alignment of the optical subsystems (fig. 1(b)). The GNRs used for the water-based colloidal suspension were synthesized by the seed-mediated approach [48, 49], PEGylated and concentrated to 4 mM Au, had

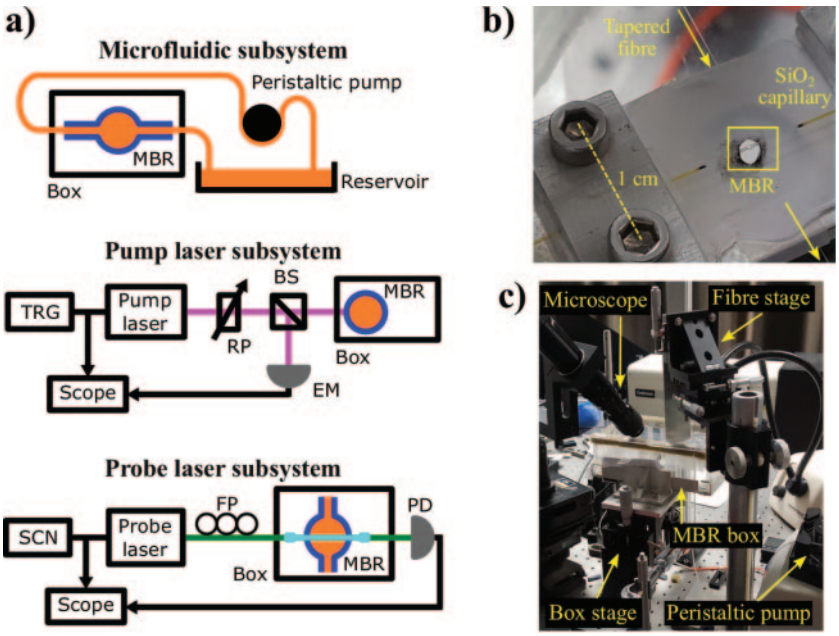

Fig. 1. – (a) Sketch of the three subsystems making up the experimental setup. The following abbreviations are used. TRG: waveform generator for pump laser triggering, RP: rotatable polariser, EM: energy meter, SCN: waveform generator for probe laser scanning, FP: fibre polarisation controller, PD: photodiode. (b) Picture of the MBR and its holder; the tapered fibre is marked by the aid of the two yellow arrows. (c) Picture of the area around the MBR box. The MBR was illuminated using a vertical configuration, with the pump laser moving from the ground up.

an average size of 70 nm × 10 nm (length × diameter) and showed a plasmonic resonance centred at 1064 nm. The microfluidic subsystem was the first to be set up during the experiment preparation.

The pump laser subsystem (fig. 1(a)) featured a free-space pulsed Nd:YAG laser (pump laser, Asclepion Laser Technologies, Jena, Germany; emission wavelength 1064 nm, pulse duration 3.3 ns, repetition rate 10 Hz, pulse energy 40 μJ) to trigger the PA emission from the GNRs. The pump laser emission was timed through an electric waveform generator (Keysight 33210A, Agilent Technologies, Santa Clara, CA, USA), which also triggered the oscilloscope (RTO1004, Rohde and Schwarz, Munich, Germany) acquisition. A rotatable polariser was placed on the beam path to tune the fluence exciting the GNRs and a beam splitter was used to monitor the fluence stability via a pyroelectric energy meter (QE8SP, Gentec-EO, Quebec, QC, Canada). The laser beam was mildly focused with a lens, obtaining a spot comparable to the MBR section (spot radius: 220 μm) and a long Rayleigh distance (7 mm). The MBR was then positioned on the waist through a set of micrometric stages moving the box containing the MBR (fig. 1(c)).

The probe laser subsystem (fig. 1(a)) used a home-made biconical tapered fibre (fig. 1(b)) to couple the emission of a CW infrared fibre laser (probe laser, Koheras ADJUSTICK, NKT Photonics, Birkerd, Denmark; spectral range 1550–1551 nm) to the MBR. A polarization controller was used to select the polarisation of the injected light and the MBR signal was collected via an InGaAs photodiode (PDA400, Thorlabs Newton, NJ, USA; bandwidth 10 MHz). A set of micrometric stages (fig. 1(c)) was used to move the fibre and, with the aid of a long working distance microscope (custom model, Navitar, Rochester, NY, USA, in fig. 1(c)) it allowed to put in contact the thin section of the fibre with the MBR equator. A second electric waveform generator (Keysight 33220A, Agilent Technologies, Santa Clara, CA, USA) allowed to finely set the probe laser wavelength and scan a frequency range up to 1 GHz (corresponding to 8 pm). The MBR and the taper were placed inside a box to avoid perturbation from air currents [50]; the box featured a glass floor so that the pump laser pulse could impinge on the MBR.

3. – Experiment description

At the beginning of the experiment the peristaltic pump was turned on to fill the MBR with the GNRs colloidal solution and, after the filling process, it was kept off for the rest of the experiment to avoid mechanical perturbation inside the MBR. Then, while observing the MBR signal (s_{opt}) via the photodiode, a WGM resonance with a high contrast was searched through a scan of the probe laser wavelength and its contrast was further increased by acting on the fiber polarisation controller (fig. 2(a), blue trace). The probe wavelength was set to the one corresponding to the half-height point ($\lambda_{\mathrm{half}} = 1550.080\,\mathrm{nm}$, $\nu_{\mathrm{half}} = c/\lambda_{\mathrm{half}}$) and the scan stopped, obtaining a flat trace (fig. 3(a), black trace) representing the baseline of the experiment. After this preparation, the pump laser was enabled and, in correspondence of each laser pulse illuminating the MBR and triggering the emission of the PA wave from the GNRs, the MBR signal changed to a pattern featuring a prominent dipolar peak followed by fast decaying oscillations (fig. 3(a), blue curve). On physical terms, this peculiar shape was the result of the PA wave acting on the MBR walls and shifting the resonance position, causing the probe laser to read a different point of the resonance fringe.

In order to retrieve the optical shift induced in the WGM resonance, which represents

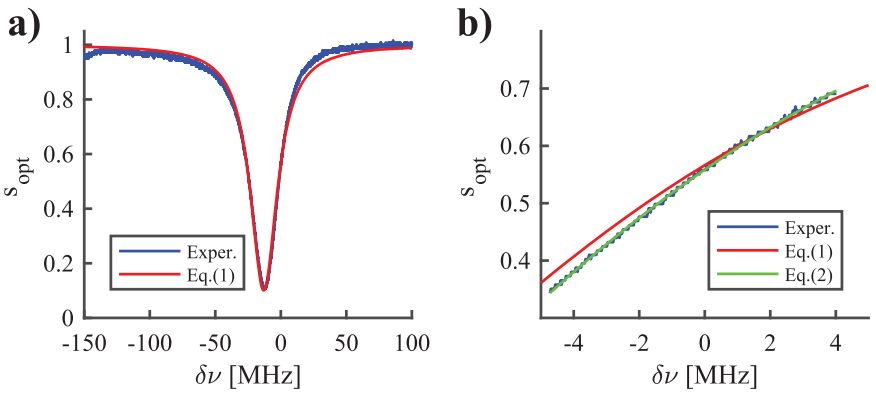

Fig. 2. – (a) WGM resonance used for the detection of the PA wave (blue curve) along with its best-fit profile using eq. (1) (red curve). (b) Detail of the fringe zone, showing the better reconstruction achieved with eq. (2).

the read-out signal of the PA wave, the transmission pattern recorded by the photodiode had to be converted into a detuning pattern. This was done by setting up a correspondence between the MBR signal s_{opt} and the detuning from the probe laser $\delta\nu$ based on the unperturbed resonance profile shown in fig. 2(a). Initially, the theoretical function for WGM profiles [51]

$$s_{\mathrm{opt}} = \frac{\left(1/\tau_{\mathrm{cp}} - 1/\tau_{\mathrm{in}}\right)^2 + 4\pi\left(\delta\nu - \delta\nu_0\right)^2}{\left(1/\tau_{\mathrm{cp}} + 1/\tau_{\mathrm{in}}\right)^2 + 4\pi\left(\delta\nu - \delta\nu_0\right)^2} \tag{1}$$

was used for this purpose, with the parameters $(\tau_{\mathrm{cp}}, \tau_{\mathrm{in}}, \delta\nu_0)$ obtained by minimizing the difference between the theoretical and the experiential profiles (fig. 2). These parameters represent the MBR-taper coupling losses, the intrinsic losses of the WGM and the WGM resonance frequency, respectively; and a detailed description is given in [51]. The procedure gave a good reconstruction of the WGM resonance on a large frequency range

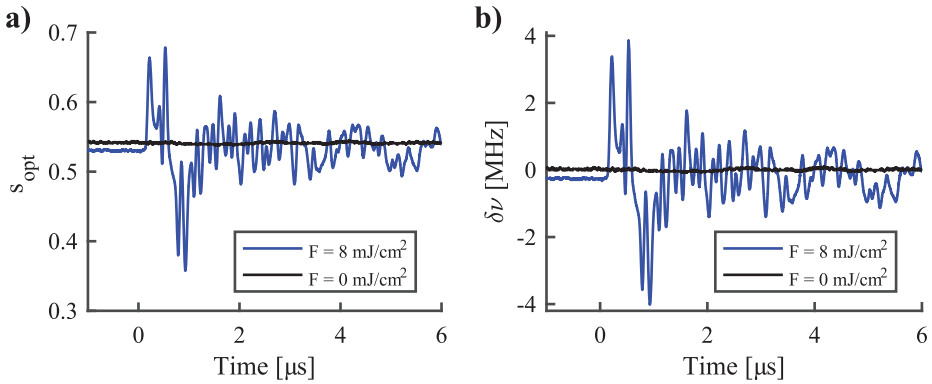

Fig. 3. – (a) MBR transmission when the GNRs PA production was not triggered (black curve) and when it was with a 8 mJ/cm^2 fluence (blue curve). (b) Results of the detuning conversion achieved by eq. (3) using the data from panel (a) as the input signals (same color code).

(fig. 2(a)), but it was not sufficiently accurate around the resonance fringe, as shown in fig. 2(b). Since the s_{opt} pattern produced by the PA wave evolved in the fringe zone (cf. blue traces of fig. 2(a) and fig. 3(a)), it was necessary to improve the s_{opt}-to-$\delta\nu$ correspondence in that zone. This was achieved by limiting the frequency range to the fringe zone and using a parabolic shape

$$s_{\text{opt}} = A(\delta\nu)^2 + B\,\delta\nu + C \tag{2}$$

instead of eq. (1). The parameters (A, B, C) were obtained by minimizing the difference between the parabola and the experiential fringe and the resulting curve allowed a precise reconstruction of the fringe (fig. 2(b), green curve). Also, using a parabola added the benefit of a simple inversion of the s_{opt}-to-$\delta\nu$ correspondence through the well-known analytical formula

$$\delta\nu = \frac{-B + \sqrt{B^2 - 4A(C - s_{\text{opt}})}}{2A}, \tag{3}$$

where the + sign was chosen instead of the − sign since λ_{half} is the half-height wavelength associated with the blue-side of the resonance.

Finally, the transmission pattern caused by the PA wave (fig. 3(a), blue curve) was inserted into eq. (3) as the s_{opt} variable, producing the blue curve shown in fig. 3(b): this detuning pattern represents the read-out of the PA wave from the MBR system and its features can be used to indirectly quantify PA wave intensity, as shown in the following. The same conversion process was also applied to a baseline trace (black curve in fig. 3(a)) obtaining the black curve in fig. 3(b), which represents a "no PA generation" reference or, in other words, the offset/background of the MBR transducer.

The typical quantity used to estimate PA wave intensity from its read-out trace is the peak-to-peak value [52]; therefore we reconstructed its trend against pump laser fluences to characterise the PA generation from GNRs, obtaining the plot shown in fig. 4(a). This trend features three excitation regimes: stable GNRs excitation and linear PA response with GNRs absorbance, up to about 10 mJ/cm^2; reshaping of GNRs into spheres and

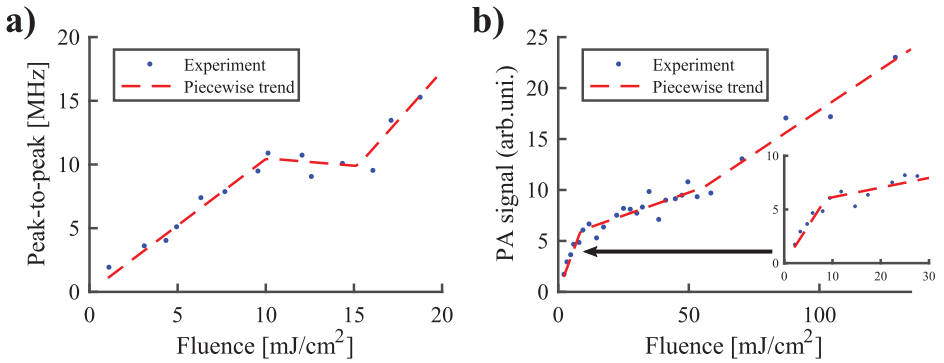

Fig. 4. – (a) Peak-to-peak value of the read-out trace obtained through the MBR system (cf. fig. 3(b)) *vs.* excitation fluence. The piecewise trend shows the three regimes of PA generation: stable excitation, reshaping, cavitation. (b) Same plot of panel (a), but here the measurements were performed with a piezoelectric microphone and GNRs were immobilized in a hydrated chitosan film (data from [53]).

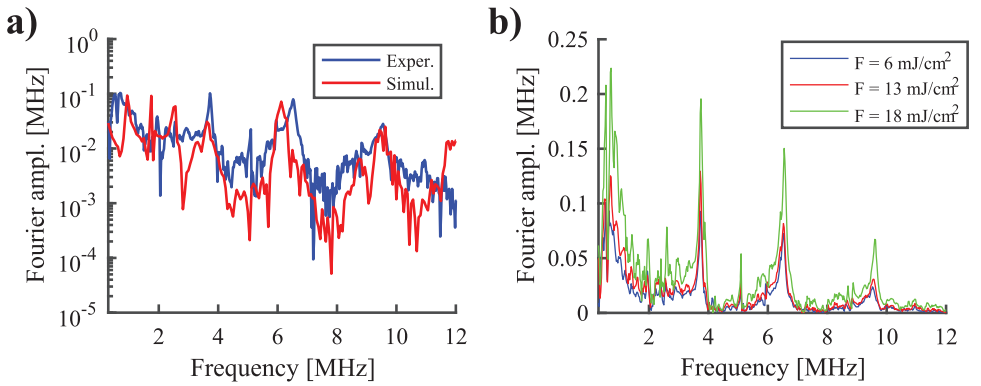

Fig. 5. – (a) Comparison between the Fourier spectrum computed from experimental data (blue curve, data from fig. 3(b)) and the one computed from the COMSOL Multiphysics® simulation results (red curve). The two curves show the same trend, further validating the MBR read-out. (b) Stability of the experimental Fourier spectrum against the change of excitation fluence.

sub-linear response from 10 up to 16 mJ/cm^2; cavitation (water evaporation in proximity of the GNRs with consequent release of a vapour shockwave) and rapid increase in PA response beyond 16 mJ/cm^2. These results are almost identical to the ones of a previous publication [53], where a standard piezoelectric transducer was used for PA detection and the GNRs were immobilized in a hydrated chitosan film (fig. 4(b)). In particular, the three regimes are found in both experiments and the reshaping threshold is practically the same; the cavitation threshold, instead, is very different, due to the different environment in which the GNRs were placed (free dispersion in water *vs.* immobilization in a chitosan film). The correct reconstruction of the GNRs response trend validates the PA read-out of the MBR system, therefore proving its implementation for the characterisation of a PA contrast agent.

Finally, another validation of the MBR system came from the comparison of the experimental PA read-out signal with a numerical simulation developed in COMSOL Multiphysics®. The simulation accounted for the cascade of thermo-elastic processes triggered by the absorption of the pump laser pulse by the GNRs, leading to the emission of the acoustic wave; then it computed the optical shift of the WGM resonance through the stress applied by the PA wave on the MBR walls (details can be found in the Supplementary Material of [41]). In fig. 5(a) the Fourier spectrum of the experimental signal from fig. 3(b) (blue curve) is compared with the one resulting from the simulation (red curve) and remarkable agreement can be found up to 11 MHz, which is on the edge of the photodiode bandwidth. Discrepancies below 0.5 MHz are a consequence of the simulation results becoming dependent on subtle mechanical details, such as the length of the silica capillary or the distance between the holder anchoring points [54]. In addition to this, the Fourier spectrum proved to stay the same regardless of the excitation fluence (fig. 5(b)), confirming that its shape is dictated by the MBR mechanical eigenmodes rather than the PA emission of the GNRs.

4. – Conclusions

The MBR system here described allowed to achieve all-optical detection of the acoustic wave generated by a PA contrast agent. The MBR read-out signal was verified both

theoretically and experimentally through a numerical simulation and a reconstruction of the GNRs photostability trend, respectively. A Fourier analysis was also performed to highlight the transduction mechanism of the MBR, which is based on its mechanical resonances.

The characteristics of the MBR system, comprising little footprint, direct implementation in a microfluidic circuit, absence of acoustic impedance-matching materials and sensitive detection, appear ideal for the realisation of mini-devices which could solve the miniaturisation problem associated with standard piezoelectric transducers. Additionally, PA detection through a mechanically resonant system could lead to low limit-of-detection thresholds, making MBRs particularly effective in non-imaging applications. This proof-of-concept experiment indeed proved the feasibility of PA detection through a MBR and work is currently underway to finalize the system for a specific task, with particular regard for biosensing, flow cytometry and material science.

* * *

This research was supported by the projects "All optical morphogenesis of nanostructures characterized by photoacoustic microscopy" (CNR - CONACyT bilateral project, 2017–2019, CONACyT Grant No. 278094) and "Microcavità Fotoniche - MiFo" (Centro Fermi). Drs. L. Cavigli, A. Fernández-Bienes, F. Ratto, S. Centi, T. García-Fernández, G. Nunzi Conti and S. Soria are gratefully acknowledged for discussion during the preparation of this paper. Mr. Franco Cosi from Istituto di Fisica Applicata "Nello Carrara" is gratefully acknowledged for the manufacturing of the tapered fibres.

REFERENCES

[1] Righini G., Dumeige Y., Feron P., Ferrari M., Nunzi Conti G., Ristic D. and Soria S., *Riv. Nuovo Cimento*, **34** (2011) 435.
[2] Matsko A. B. and Ilchenko V. S., *IEEE J. Sel. Top. Quantum Electron.*, **12** (2006) 3.
[3] Ilchenko V. S. and Matsko A. B., *IEEE J. Sel. Top. Quantum Electron.*, **12** (2006) 15.
[4] Savchenkov A. A., Matsko A. B., Ilchenko V. S. and Maleki L., *Opt. Express*, **15** (2007) 6768.
[5] Collodo M. C., Sedlmeir F., Sprenger B., Svitlov S., Wang L. J. and Schwefel H. G. L., *Opt. Express*, **22** (2014) 19277.
[6] Lin G., Coillet A. and Chembo Y. K., *Adv. Opt. Photon.*, **9** (2017) 828.
[7] Sandoghdar V., Treussart F., Hare J., Lefèvre-Seguin V., Raimond J. M. and Haroche S., *Phys. Rev. A*, **54** (1996) R1777.
[8] Matsko A. B., Maleki L., Savchenkov A. A. and Ilchenko V. S., *J. Mod. Opt.*, **50** (2003) 2523.
[9] Kippenberg T. J., Holzwarth R. and Diddams S. A., *Science*, **332** (2011) 555.
[10] Foreman M. R., Swaim J. D. and Vollmer F., *Adv. Opt. Photon.*, **7** (2015) 168.
[11] Vollmer F. and Arnold S., *Nat. Methods*, **5** (2008) 591.
[12] Avino S., Krause A., Zullo R., Giorgini A., Malara P., De Natale P., Loock H. P. and Gagliardi G., *Adv. Opt. Mater.*, **2** (2014) 1155.
[13] He L., Özdemir Ş. K., Zhu J., Kim W. and Yang L., *Nat. Nanotechnol.*, **6** (2011) 428.
[14] Sumetsky M., Dulashko Y. and Windeler R. S., *Opt. Lett.*, **35** (2010) 898.
[15] Berneschi S., Farnesi D., Cosi F., Nunzi Conti G., Pelli S., Righini G. C. and Soria S., *Opt. Lett.*, **36** (2011) 3521.
[16] Watkins A., Ward J., Wu Y. and Chormaic S. N., *Opt. Lett.*, **36** (2011) 2113.
[17] Righini G. and Soria S., *Sensors*, **16** (2016) 905.
[18] Berneschi S., Baldini F., Cosci A., Farnesi D., Nunzi Conti G., Tombelli S., Trono C., Pelli S. and Giannetti A., *Sens. Actuators B: Chem.*, **242** (2017) 1057.

[19] Li M., Wu X., Liu L., Fan X. and Xu L., *Anal. Chem.*, **85** (2013) 9328.
[20] Hogan L. T., Horak E. H., Ward J. M., Knapper K. A., Nic Chormaic S. and Goldsmith R. H., *ACS Nano*, **13** (2019) 12743.
[21] Li Z., Zhu C., Guo Z., Wang B., Wu X. and Fei Y., *Micromachines*, **9** (2018) 274.
[22] Han K., Zhu K. and Bahl G., *Appl. Phys. Lett.*, **105** (2014) 014103.
[23] Chen Z., Wu X., Liu L. and Xu L., *Sensors*, **17** (2017) 2256.
[24] Hyun Kim K., Bahl G., Lee W., Liu J., Tomes M., Fan X. and Carmon T., *Light Sci. Appl.*, **2** (2013) e110.
[25] Chen Z., Li M., Wu X., Liu L. and Xu L., *Opt. Express*, **23** (2015) 17659.
[26] Beard P., *Interface Focus*, **1** (2011) 602.
[27] Emelianov S. Y., Li P.-C. and O'Donnell M., *Phys. Today*, **62** (2009) 34.
[28] Wang L. V. and Hu S., *Science*, **335** (2012) 1458.
[29] Manohar S., Kharine A., van Hespen J. C. G., Steenbergen W. and van Leeuwen T. G., *Phys. Med. Biol.*, **50** (2005) 2543.
[30] Xu M. and Wang L. V., *Rev. Sci. Instrum.*, **77** (2006) 041101.
[31] Razansky D., Vinegoni C. and Ntziachristos V., *Opt. Lett.*, **32** (2007) 2891.
[32] Strohm E. M., Moore M. J. and Kolios M. C., *IEEE J. Sel. Top. Quantum Electron.*, **22** (2016) 137.
[33] Wang L. V., *Photoacoustic Imaging and Spectroscopy* (CRC Press, Boca Raton) 2009.
[34] Morse P. M. and Uno Ingard K., *Theoretical Acoustics* (Princeton University Press, Princeton, New Jersey) 1986.
[35] Safari A. and Akdogan E. K., *Piezoelectric and Acoustic Materials for Transducer Applications* (Springer US) 2008.
[36] Li M., Tang Y. and Yao J., *Photoacoustics*, **10** (2018) 65.
[37] Wissmeyer G., Pleitez M. A., Rosenthal A. and Ntziachristos V., *Light Sci. Appl.*, **7** (2018) 53.
[38] Kim K. H., Luo W., Zhang C., Tian C., Guo L. J., Wang X. and Fan X., *Sci. Rep.*, **7** (2017) 109.
[39] Dong B., Li H., Zhang Z., Zhang K., Chen S., Sun C. and Zhang H. F., *Optica*, **2** (2015) 169.
[40] Chen S.-L., Guo L. J. and Wang X., *Photoacoustics*, **3** (2015) 143.
[41] Frigenti G., Cavigli L., Fernández-Bienes A., Ratto F., Centi S., García-Fernández T., Nunzi Conti G. and Soria S., *Phys. Rev. Appl.*, **12** (2019) 014062.
[42] Eghtedari M., Oraevsky A., Copland J. A., Kotov N. A., Conjusteau A. and Motamedi M., *Nano Lett.*, **7** (2007) 1914.
[43] Agarwal A., Huang S. W., ODonnell M., Day K. C., Day M., Kotov N. and Ashkenazi S., *J. Appl. Phys.*, **102** (2007) 064701.
[44] Zhang Q., Iwakuma N., Sharma P., Moudgil B. M., Wu C., McNeill J., Jiang H. and Grobmyer S. R., *Nanotechnology*, **20** (2009) 395102.
[45] Chamberland D. L., Agarwal A., Kotov N., Fowlkes J. B., Carson P. L. and Wang X., *Nanotechnology*, **19** (2008) 095101.
[46] García-Álvarez R., Chen L., Nedilko A., Rix A., Lederle W., Pathak V., Lammers T., von Plessen G., Kostarelos K., Liz-Marzían L. M., Kuehne A. J. C. and Chigrin D. N., *ACS Photonics*, **7** (2020) 646.
[47] Kumar P. S., Pastoriza-Santos I., Rodríguez-González B., de Abajo F. J. G. and Liz-Marzán L. M., *Nanotechnology*, **19** (2007) 015606.
[48] Vigderman L. and Zubarev E. R., *Chem. Mater.*, **25** (2013) 1450.
[49] Cavigli L., Centi S., Borri C., Tortoli P., Panettieri I., Streit I., Ciofini D., Magni G., Rossi F., Siano S., Ratto F. and Pini R., *J. Biophotonics*, **12** (2019) e201900082.
[50] Cosci A., Berneschi S., Giannetti A., Farnesi D., Cosi F., Baldini F., Nunzi Conti G., Soria S., Barucci A., Righini G. *et al.*, *Sensors*, **16** (2016) 1405.
[51] Frigenti G., Arjmand M., Barucci A., Baldini F., Berneschi S., Farnesi D., Gianfreda M., Pelli S., Soria S., Aray A., Dumeige Y., Féron P. and Nunzi Conti G., *J. Opt.*, **20** (2018) 065706.

[52] Cavigli L., Tatini F., Borri C., Ratto F., Centi S., Cini A., Lelli B., Matteini P. and Pini R., *J. Vis. Exp.*, **111** (2016) e53328.
[53] Cavigli L., Centi S., Lai S., Borri C., Micheletti F., Tortoli P., Panettieri I., Streit I., Rossi F., Ratto F. and Pini R., *Light and ultrasound activated microbubbles around gold nanorods for photoacoustic microsurgery*, in *Proceedings of Opto-Acoustic Methods and Applications in Biophotonics III*, edited by Ntziachristos V. and Zemp R., Vol. **10415** (International Society for Optics and Photonics (SPIE)) 2017, pp.9–13.
[54] Roselló-Mechó X., Farnesi D., Frigenti G., Barucci A., Fernández-Bienes A., García-Fernández T., Ratto F., Delgado-Pinar M., Andrés M. V., Nunzi Conti G. and Soria S., *Sci. Rep.*, **9** (2019) 7163.